Article

# Enhancing catalytic durability in alkaline oxygen evolution reaction through squaric acid anion intercalation

Ruoyao Fan[1,4], Shanshan Lu[2,4], Fuli Wang[1], Yusheng Zhang[1], Mirabbos Hojamberdiev[3], Yongming Chai[1] ✉, Bin Dong [1] ✉ & Bin Zhang [2] ✉

The corrosive acidic interfacial microenvironment caused by rapid multi-step deprotonation of alkaline oxygen evolution reaction in industrial high current water electrolysis is one of the key problems limiting its stability. Some functional anions derived from electrocatalysis exhibit special functionalities in modulating the interface microenvironment, but this matter has not received adequate attention in academic discussions. Here we show that the coordinate squaric acid undergoes a dissolve-re-intercalation process in alkaline oxygen evolution, leading to its stabilization within the Fe-doped NiOOH interlayer in the form of the squaric acid anions (NiFe-SQ/NF-R). These intercalated squaric acid anions stabilizes $OH^-$ through multiple hydrogen bond interactions, which is conducive to maintaining high catalytic interface alkalinity. Hence, the interfacial acidification of prepared NiFe-SQ/NF-R is inhibited, resulting in a tenfold prolong in its catalytic durability (from 65 to 700 h) when exposed to 3.0 A cm$^{-2}$, as opposed to NiFe-LDH/NF-R. This derived functional anion guarantees the enduring performance of the NiFe-derived electrocatalyst under high current densities by controlling the interfacial alkalinity.

With the rapid expansion of the hydrogen energy industry and the wide application of large-scale water electrolyzers,[1–3] the microenvironmental effect between the electrode and electrolyte interface[4,5] in industrial-scale devices has increased. In large-scale, high-current, and compact water electrolysis systems, the relationship between the influence of special material transformation pathways, ion conduction modes, and interfacial molecule/ion interaction on the local microenvironment of electrodes and the catalytic performance remains unexplored. Further regulation of the dynamic interface microenvironment will help to enhance the selectivity and reaction rate of some catalytic processes, which provides an idea for further improving the activity and stability of electrocatalysts.

Ni-Fe-based (oxy)hydroxide stands out as a widely favored electrocatalyst for the oxygen evolution reaction (OER) under alkaline conditions.[6–8] Numerous endeavors have been undertaken to bolster its catalytic performance through methods such as element doping[9–11], morphology manipulation[12,13], strain adjustment[14], and various other approaches. However, the catalytic interface microenvironment can also have a drastic impact on the apparent catalytic performance.[15,16] The focus on the catalyst in the microstructure design alone may prove insufficient to fulfill the demands of practical application requirements. In the violent reaction process of high-current water electrolysis, the multistep deprotonation of the alkaline OER initiates the rapid formation and local accumulation of H$^+$, resulting in the formation of an acidic interfacial microenvironment. This local acidic microenvironment is strongly corrosive to the metal site of Ni-Fe-based (oxy)hydroxide, posing a challenge to enhancing its performance and durability.[17–19] As a consequence, promoting the swift

[1]State Key Laboratory of Heavy Oil Processing, College of Chemistry and Chemical Engineering, China University of Petroleum (East China), Qingdao, China. [2]Department of Chemistry, School of Science, Tianjin University, Tianjin, China. [3]Mads Clausen Institute, University of Southern Denmark, Sønderborg, Denmark. [4]These authors contributed equally: Ruoyao Fan, Shanshan Lu. ✉e-mail: ymchai@upc.edu.cn; dongbin@upc.edu.cn; bzhang@tju.edu.cn

transformation and consumption of $H^+$ is essential for addressing the abovementioned acid corrosion issue, ensuring favorable alkalinity at the anode interface, and further enhancing catalytic activity and stability, particularly during large-current electrolysis operations.

While some studies have demonstrated that breaking down Ni-Fe layered double hydroxides (NiFe-LDH) into thin nanosheets[20] or initiating element leaching to loosen the catalyst's outer layer[21] can promote the diffusion of $OH^-$ as a proton acceptor to slow the formation of a local acidic microenvironment, the challenge now lies in quickly and adequately consuming such a large amount of $H^+$ under a large current. Recent studies by Ranit Ram show that defect structures induced by selectively dissolved $WO_4^{2-}$ ions have the capability to trap and preserve $H_2O$ and $OH^-$, thus prolonging the catalytic activity of OER electrocatalysts in acidic conditions.[22] Motivated by this discovery, our research aims to incorporate specific functional compounds known as "intermediaries" to stabilize $OH^-$ at the electrochemical interface, addressing the challenge of anodic acidification in high-current alkaline OER processes.

Herein, we prepared a squaric acid anion ($Sq^{2-}$) modified Fe-doped NiOOH as a derived catalytic active layer to drive alkaline OER catalytic processes with ampere-scale currents. Due to the spatial volume effect of $Sq^{2-}$, the increase in the layer spacing of Fe-doped NiOOH promotes the effective diffusion of $OH^-$, which increases the concentration of $OH^-$ near the active sites and thus enhances the catalytic activity. The intercalation adsorbed $Sq^{2-}$ has been found to stabilize $OH^-$ of the interface through multiple hydrogen bonding interactions, thereby preserving a high interface alkalinity, which plays a critical role in prolonging the catalytic lifespan, particularly in instances of large current densities. Thus, the NiFe-SQ/NF-R electrode created in this research exhibits a low overpotential of 284 mV to reach 1.0 A cm$^{-2}$ and demonstrates a remarkably large current stability surpassing 700 h at 3.0 A cm$^{-2}$. This work demonstrates the feasibility of using the stabilization effect of functional anions on $OH^-$ to maintain high anode interface alkalinity and improve catalytic activity and stability, paving the way for the innovative design of large-scale current OER electrocatalysts for industrial applications.

## Results

### Structural design and characterization

The importance of designing more stable large-current OER electrocatalysts from the perspective of improving the local anode alkalinity or weakening the acidic interfacial microenvironment has not been widely recognized, and there is a lack of comprehensive research and literature in this area. Therefore, to further prolong the actual service life and increase the large current resistance of anode electrocatalysts in industrial water electrolyzers, an effective strategy and innovative mechanisms for designing catalyst structures based on real interfacial microenvironments are urgently needed. We are dedicated to developing a more practical Ni-Fe-based alkaline OER electrocatalyst by focusing on improving its activity and stability at large current densities. Our efforts involved creating a consolidated integrated anode using nickel foam (NF) as the self-supporting base and etched substrate.[23,24] As illustrated in Fig. 1a, the Ni-Fe bimetallic squarate-based coordination polymer (NiFe-SQ/NF) was synthesized through a one-step hydrothermal process involving in situ etching of NF with the help of an acidic environment facilitated by SQ, Fe(NO$_3$)$_3$·9H$_2$O, and polyvinyl pyrrolidone (PVP) solution (Supplementary Table 1). Additional detailed synthesis procedures and reaction equations for the etching processes can be found in the experimental methods section and in the notes section of Supplementary Fig. 1. As shown in Fig. 1b, NiFe-SQ/NF exhibited a distinct cuboid angular stack structure, growing uniformly and closely on the initially smooth NF surface (Supplementary Fig. 2). The scanning electron microscopy (SEM)-mapping images show that Fe, Ni, O and C elements are uniformly distributed on the surface of NiFe-SQ/NF (Supplementary Fig. 3). The

analysis conducted using inductively coupled plasma-optical emission spectroscopy (ICP-OES) revealed that the ratio of iron to nickel in the NiFe-SQ/NF sample was approximately 0.39 (Supplementary Table 2). The typical square structure of the squarate-based coordination polymer is only achievable through the inclusion of ferric nitrate during the synthesis process (Supplementary Fig. 4), which highlights the significance of the purple Fe-based complex and the acidic conditions in facilitating the production of NiFe-SQ/NF. The samples synthesized without ferric nitrate (Ni-SQ/NF-R) showed poor catalytic activity (Supplementary Fig. 5). X-ray diffraction (XRD) analysis of NiFe-SQ/NF reveals distinctive peaks associated with the Ni-Fe coordination polymer (NiFe(H$_2$O)$_2$(C$_4$O$_4$))[25–27] and metallic Ni (PDF# 96-210-0644) (Supplementary Fig. 6), suggesting a straightforward phase composition. Then, cyclic voltammetry (CV) was utilized to initiate the rapid surface electrochemical reconstruction activation process of NiFe-SQ/NF, and NiFe-SQ/NF-R was obtained. Only the peaks of metal Ni were detected in the XRD pattern of NiFe-SQ/NF-R, which may be attributed to the presence of numerous amorphous metal hydroxide/hydroxyl oxide species within the surface reconfigurable layer. Alkaline hydrolysis occurs on the surface of NiFe-SQ/NF during electrochemical anodic activation treatment, causing some $Sq^{2-}$ to run off and creating a net-like fissure structure in NiFe-SQ/NF-R (Fig. 1c). These fissures act as beneficial micron-scale channels that increase gas release and electrolyte flux at the electrode surface, particularly under large current conditions. A comparison of the water contact angles of the NiFe-SQ/NF and NiFe-SQ/NF-R surfaces reveals that the electrochemical activation treatment shifts the catalytic surface from hydrophobic to superhydrophilic (Supplementary Fig. 7), promoting rapid wetting and electrolyte diffusion on the electrode. In Supplementary Fig. 8, the SEM maps of NiFe-SQ/NF-R show no elemental aggregation, indicating that the electrochemical treatment only excites the superficial species without changing the main structure. SEM images of NiFe-SQ/NF-R sample cross-section after OER show that the square catalyst is closely bound to the outer surface of the nickel foam (Supplementary Fig. 9). This self-etching growth strategy ensures strong adhesion at the interface between catalyst and substrate.

The electrochemical oxidation reconstruction and the dissolution of the squaric acid ligand were carried out simultaneously. The dissolution of squaric acid results in an increased presence of defects in the restructured framework (NiFe-SQ/NF-R), which in turn accelerates deeper reconstruction process.[28,29] To illustrate this phenomenon, a comparison was conducted between the electrolyte after CV activation and the KOH solution of $Sq^{2-}$, revealing that they have similar Raman characteristic peaks attributed to $Sq^{2-}$ (Supplementary Fig. 10).[30,31] To further investigate the more subtle structural transformation of NiFe-SQ/NF during electrochemical activation, we performed an in-depth examination of the sample using spherical aberration-corrected transmission electron microscopy (AC-TEM). Specifically, in Fig. 1d, short and disordered lattice fringes can be observed in the outer reconstructed layer of NiFe-SQ/NF-R, which are attributed to metallic hydroxyl oxides. More comprehensive AC-TEM images of NiFe-SQ/NF-R are shown in Supplementary Fig. 11. Following the formation of this special crystalline-amorphous composite layer, the reconstruction process can be terminated quickly, serving as a protective barrier for the internal coordination polymerization structure. The selected-area electron diffraction pattern (Supplementary Fig. 12) for NiFe-SQ/NF-R exhibits similar structural information that matches that of r-NiOOH (PDF# 00-006-0075). Under the same test conditions, NiFe-LDH/NF-R exhibits a longer-range ordered distribution of the (1 0 1) crystal plane (Supplementary Fig. 13), which corresponds to its XRD (PDF# 00-040-0215, Supplementary Fig. 14). The NiFe-LDH/NF composite discussed in this study was prepared using a conventional hydrothermal method.[32,33] The in situ Raman analysis revealed that the NiFe-LDH/NF experienced a reconstruction process under the excitation of oxidation current, leading to the gradual transformation of Ni(OH)$_2$ (455, 530 cm$^{-1}$) into (Fe-doped) NiOOH (475,
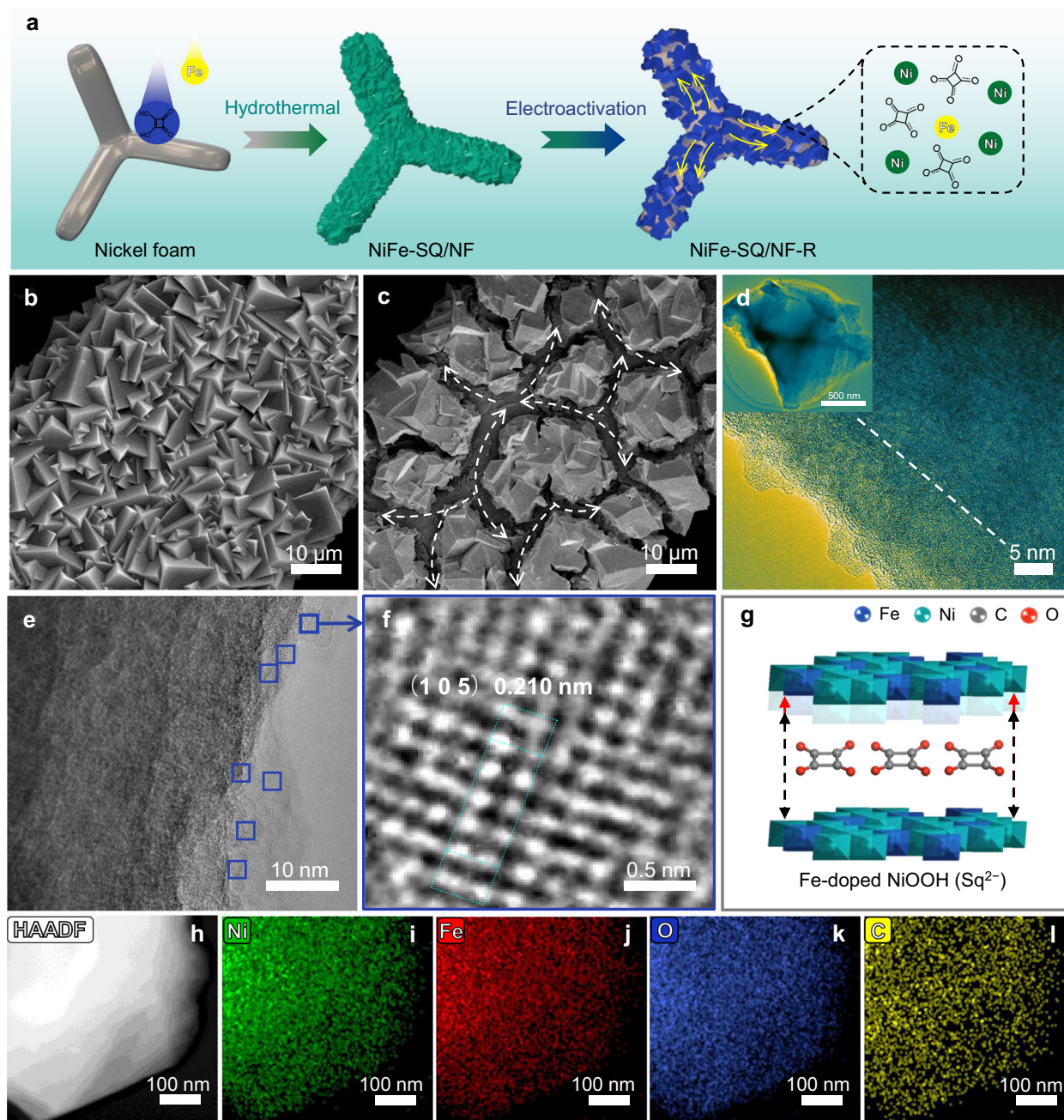
**Fig. 1 | Synthesis strategy and physical characterization of NiFe-SQ/NF-R.** **a** Diagram of the preparation process of NiFe-SQ/NF-R. SEM images of **b** NiFe-SQ/NF and **c** NiFe-SQ/NF-R. **d** AC-TEM images with color processing of NiFe-SQ/NF-R (Taken from the square morphology region). **e** AC-TEM image of NiFe-SQ/NF-R. **f** The corresponding autocorrelated lattice fringe pattern of NiOOH(Sq$^{2-}$) (1 0 5). **g** Structure diagram of Fe-doped NiOOH(Sq$^{2-}$) (Green, blue, red, and gray represent the Ni, Fe, O, and C atoms). **h** HAADF TEM image and **i–l** elemental mappings of Ni, Fe, O, and C elements for NiFe-SQ/NF-R.

550 cm$^{-1}$) (Supplementary Fig. 15). This indicates that NiFe-LDH/NF and NiFe-SQ/NF produce similar NiOOH components after electrochemical reconstruction, which is recognized as an active species of OER. The standard spacing of NiOOH (1 0 5) crystal faces is typically measured at 0.209 nm according to statistical data of PDF (# 00-006-0075). However, our actually observations show that the (1 0 5) crystal face of unintercalated NiOOH produced by electrochemical activation is slightly smaller at 0.205 nm under identical test conditions (Supplementary Fig. 16). The small gap with the standard values could potentially be attributed to inevitable structural strain induced by electrochemical activation during the preparation process. The presence of Sq$^{2-}$ insertion leads to a noticeable broadening of the (1 0 5) crystal face of NiOOH, measuring at 0.210 nm as indicated by the blue frame in Fig. 1e, f when compared to the NiOOH (1 0 5) crystal face without Sq$^{2-}$ (0.205 nm). At the same time, the NiOOH in-situ Raman characteristic peaks of NiFe-SQ/NF also show peak shift caused by intercalated Sq$^{2-}$ (Supplementary Fig. 17). The results above demonstrate that the Sq$^{2-}$ intercalation-modified Fe-doped NiOOH obtained by electrochemical directional reconstruction results in a larger layer space (Fig. 1g), serving as a wide electrolyte diffusion channel and an ideal reaction region. The element mapping images of NiFe-SQ/NF-R under high-resolution AC-TEM reveal a homogeneous distribution of Ni, Fe, O, and C (Fig. 1h–l), suggesting that the electrochemical activation treatment does not lead to phase segregation of the catalytic components.
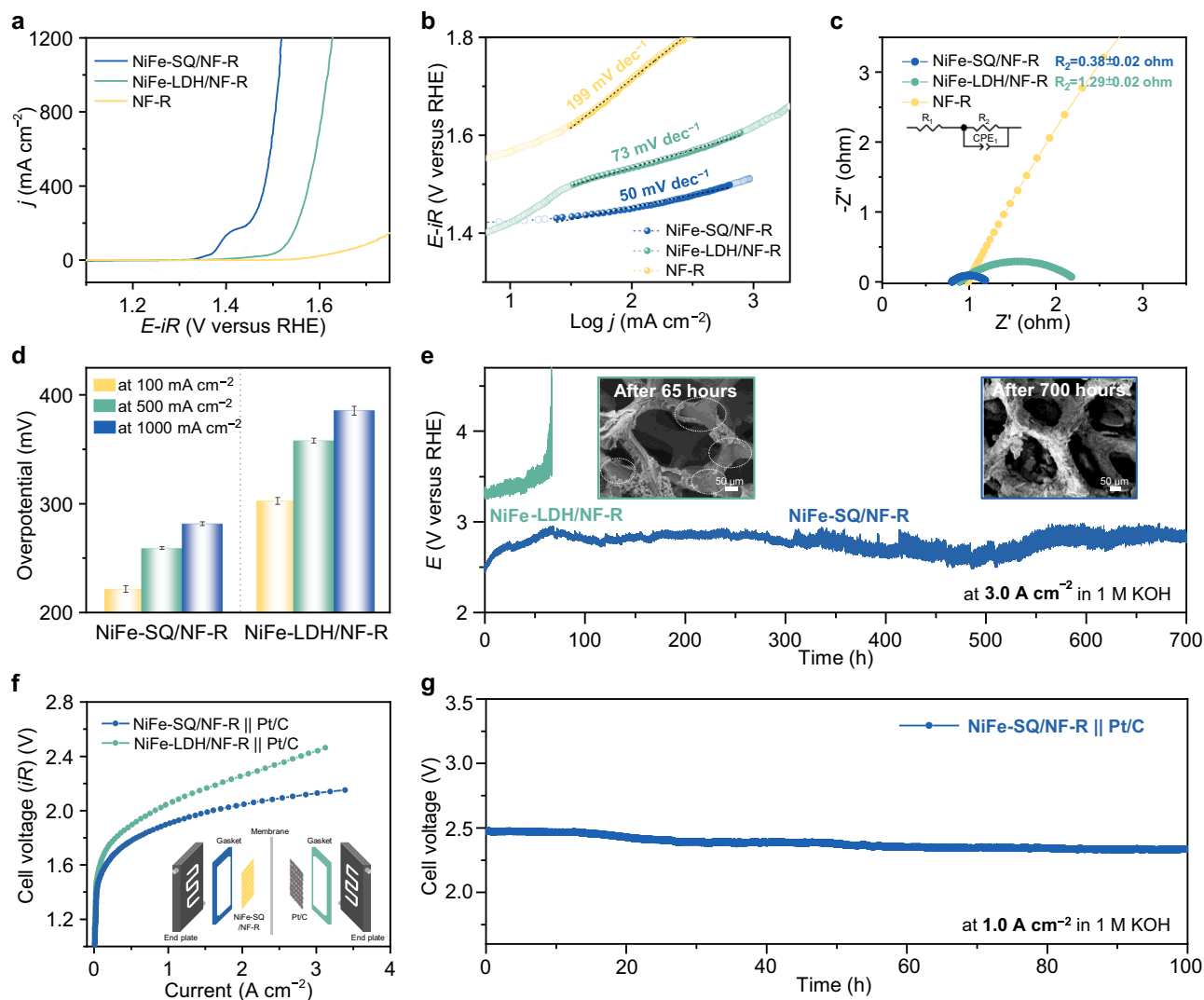
**Fig. 2 | Enhanced catalytic activity and stability of OER at high currents. a** LSV curves for NiFe-SQ/NF-R, NiFe-LDH/NF-R, and NF-R in 1 M KOH at a scan rate of 5.0 mV s$^{-1}$ with $iR$-correction, where the system solution resistance values ($R_1$) was measured to be 0.80 ± 0.02, 0.89 ± 0.02 and 0.99 ± 0.02 Ω. **b** The corresponding Tafel slopes. **c** Nyquist diagram of NiFe-SQ/NF-R, NiFe-LDH/NF-R, and NF-R at a constant potential of 1.48 V versus RHE. **d** Overpotentials of NiFe-SQ/NF-R and NiFe-LDH/NF-R at 100 mA cm$^{-2}$, 500 mA cm$^{-2}$ and 1000 mA cm$^{-2}$. The error bars are means ± standard deviation (3 replicates). **e** Long-term CP test (without $iR$

compensation) of the samples at a current density of 3.0 A cm$^{-2}$. The illustrations are SEM images of NiFe-LDH/NF-R and NiFe-SQ/NF-R after 65 h and 700 h of stability testing, respectively. **f** Polarization curves of the assembled NiFe-SQ/NF-R(+) || Pt/C(−) and NiFe-LDH/NF-R(+) || Pt/C(−) AEMWEs. The inset image is a schematic diagram of the PEMWE electrode structure. **g** Stability test of AEMWE cells assembled with NiFe-SQ/NF-R electrodes at 1.0 A cm$^{-2}$ (without $iR$ compensation). Source data are provided as a Source Data file.

## Electrocatalytic oxygen evolution reaction performance

The electrochemical properties of all samples in standard three-electrode and membrane electrode systems were investigated in depth. Purified KOH was used as the electrolyte during the test. Supplementary Fig. 18 displays that the fast surface reconstruction process driven by electrochemistry allows the catalytic surface to achieve a state of relative equilibrium after ten CV activations, exhibiting consistent and stable catalytic properties. In Fig. 2a, NiFe-SQ/NF-R demonstrates desirable overpotentials of 261 mV and 284 mV to achieve the current densities of 500 mA cm$^{-2}$ and 1000 mA cm$^{-2}$ positioning it as a leading electrocatalyst for efficient OER at large current levels, which are lower than that of NiFe-LDH/NF-R (Fig. 2d). The non-$iR$ corrected voltammograms for these three electrocatalysts is shown in Supplementary Fig. 19. Based on the previously mentioned results, we believe that such notable catalytic properties are due to micron-scale transport channels, wider layer spaces, and faster catalytic reaction kinetics, which are caused by Sq$^{2-}$ intercalation. Comparative

experiments (Supplementary Fig. 20) were carried out to confirm the limited influence of Sq$^{2-}$ adsorption at the catalytic interface on the catalytic performance of the OER. The augmentation of Sq$^{2-}$ did not result in a noteworthy rise in the oxidation current, which also proves from the side that Sq$^{2-}$ will not be further oxidized in an alkaline environment. Upon comparing the LSV curves of NiFe-SQ/NF-R and NiFe-LDH/NF-R, NiFe-SQ/NF-R exhibits notably larger Ni$^{2+}$/Ni$^{3+}$ oxidation peaks, suggesting that the intercalation effect of Sq$^{2-}$ can promote the formation and stabilization of NiOOH.[34,35] The reduced Tafel slope observed for NiFe-SQ/NF-R (50 mV dec$^{-1}$) (Fig. 2b) indicates that the presence of intercalated adsorbed Sq$^{2-}$ enhances the catalytic reaction kinetics. The interfacial charge transfer capability of the samples was assessed using electrochemical impedance spectroscopy (EIS). NiFe-SQ/NF-R exhibited the smallest charge transfer resistance ($R_{ct}$) (Fig. 2c), which suggests that the interlayer Sq$^{2-}$ facilitates rapid transfer of the interface charge to enhance the OER. The electrochemical active surface area (ECSA) of NiFe-SQ/NF-R (99.75 cm$^2$) and

NiFe-LDH/NF-R (46.00 cm$^2$) was determined from CV curves at different sweep speeds (Supplementary Fig. 21a–c). Analysis of the polarization curves normalized by the ECSA reveals that NiFe-SQ/NF-R demonstrates higher intrinsic catalytic activity (Supplementary Fig. 21d). The Faraday efficiency is calculated by measuring the volume of oxygen produced by the NiFe-SQ/NF-R during electrolysis (drainage method). The experimental findings, illustrated in Supplementary Fig. 22, exhibit a notable proximity between the observed data and the theoretical values derived from Faraday's principles of electrolysis. This yields a Faraday efficiency nearing 96 (±0.86) %, suggesting that the augmented current density stems from the OER process. In other words, the outstanding alkaline OER performance of NiFe-SQ/NF-R is mainly attributed to the intercalation of Sq$^{2-}$, which promotes increased NiOOH generation, increases OH$^-$ diffusion channels, expedites interfacial electron transfer, and provides higher intrinsic catalytic activity. The CoFe-SQ/CF-R and Fe-SQ/IF-R samples were effectively synthesized through similar methods using cobalt foam (CF) and iron foam (IF) (Supplementary Fig. 23). Our proposed synthesis method has been validated for universal applicability, making it well-suited for widespread industrial implementation.

The multistep chronopotentiometry (CP) step test diagram illustrates that NiFe-SQ/NF-R can adjust to fluctuating current (Supplementary Fig. 24a). Additionally, NiFe-SQ/NF-R can maintain stable catalytic performance for more than 100 h at consistent current densities of 100 mA cm$^{-2}$ and 500 mA cm$^{-2}$ (Supplementary Fig. 24b) while retaining its original catalytic structure even after this duration (Supplementary Fig. 24c–f). The catalytic activities of NiFe-SQ/NF-R and NiFe-LDH/NF-R were evaluated at different temperatures (Supplementary Fig. 25a, b) due to the observed increase in the local temperature near the anode under high current density conditions. The findings revealed a considerable enhancement in the catalytic activity of both compounds with increasing temperature. To mitigate the influence of temperature, rigorous measures were taken to maintain a consistent temperature by utilizing a temperature-equalizing apparatus during high-current assessments. Analysis of the Arrhenius plot indicated that NiFe-SQ/NF-R exhibited a lower apparent electrochemical activation energy (Ea)[36] than did NiFe-LDH/NF-R (Supplementary Fig. 25c). Further examination was conducted on the long-term stability of NiFe-SQ/NF-R and NiFe-LDH/NF-R when subjected to a persistent large current density of 3.0 A cm$^{-2}$. As depicted in Fig. 2e, conventional NiFe-LDH/NF-R can only endure ~65 h of CP testing at 3.0 A cm$^{-2}$, whereas NiFe-SQ/NF-R exhibits notable stability for more than 700 h. After observing the surface morphology of the electrocatalysts before and after the large-current stability test using SEM, despite undergoing 700 h of high-current testing, the surface structure of NiFe-SQ/NF-R does not exhibit obvious dissolution or large areas falling off, a stark difference from the incomplete catalytic surface of NiFe-LDH/NF-R after 65 h of testing (illustration of Fig. 2e). While some potassium salt deposits are visible on the surface of NiFe-SQ/NF-R during the drying process, altering its morphology is not expected to greatly impact its stability. In addition, under industry-relevant conditions (30 wt% KOH, 60 °C), NiFe-SQ/NF-R also exhibits lower battery voltages and better stability than typical NiFe-LDH/NF-R (Supplementary Fig. 26). And under simulated industrial conditions, the NiFe-SQ/NF-R we prepared is comparable to other reported catalytic electrodes (Supplementary Table 3). Therefore, the sudden deactivation of NiFe-LDH/NF-R is mainly due to the structural collapse and surface degradation caused by acidic interfacial microenvironment. Building upon the preceding characterization findings, it is deduced that the distinctive function of intercalated Sq$^{2-}$ in upholding high interface alkalinity results in the preservation of the structural integrity of NiFe-SQ/NF-R, enhancing its stability notably under high current conditions. Next, we integrated NiFe-SQ/NF-R as a self-supporting anode into an anion exchange membrane water electrolyzer (AEMWE) to investigate the comprehensive performance of water electrolysis. For the cathode, we selected the Pt/C electrocatalyst, whose performance is shown in Supplementary Fig. 27. Notably, Fig. 2f illustrates that the NiFe-SQ/NF-R electrode outperforms the NiFe-LDH/NF-R electrode, operating at a lower cell voltage of 2.13 V to achieve a large current of 3.0 A cm$^{-2}$, compared to the requirement of 2.44 V for NiFe-LDH/NF-R. Compared to findings in other research studies, the utilization of AEMWE to attain such elevated levels of current density stands as a cutting-edge approach (Supplementary Table 4). The AEMWE combined with NiFe-SQ/NF-R demonstrates stability under high current density of 1.0 A cm$^{-2}$, suggesting promising application prospects within membrane electrode systems (Fig. 2g).

## The structural source of long-term stability for high currents

The strong dissolution tendency of Fe elements in the OER process is also one of the important factors affecting the stability of OER electrocatalysts.[37,38] Consequently, a meticulous analysis of the electronic environment and coordination configuration of NiFe-SQ/NF-R is carried out utilizing X−ray photoelectron spectroscopy (XPS) and X-ray absorption fine structure energy spectrum (XAFS) methodologies. The results depicted in Fig. 3a illustrate a slight shift in the Ni$^{2+}$ 2$p_{3/2}$ and Ni$^{3+}$ 2$p_{3/2}$ peaks between NiFe-SQ/NF-R and NiFe-LDH/NF-R, implying a closely resembling electronic configuration surrounding the Ni sites in both. Nonetheless, discernible distinctions were observed in the Fe sites environment between the two. In the K-edge XANES spectrum of Fe, compared with NiFe-LDH/NF-R, the pre-edge peak intensity of NiFe-SQ/NF-R is increased, indicating that there are coordination vacancies near the Fe sites[39] (Fig. 3b). The wavelet transform (WT) contour map of NiFe-SQ/NF-R illustrates unique coordination features linked to Fe-O and Fe-M (Fig. 3c). In more detail, the K-edge extended X-ray absorption fine structure (EXAFS) spectra of Fe shows that the characteristic peaks attributed to both Fe-O (1.5 Å) and Fe-M (2.7 Å) shells in NiFe-SQ/NF-R show obvious downward trends (Fig. 3d). Upon examination, it was determined that the coordination number in proximity to the Fe sites within NiFe-SQ/NF-R exhibited a notable decrease compared to that near the Fe sites in NiFe-LDH/NF-R (Supplementary Table 5). This disparity is linked to the emergence of vacancies surrounding the Fe site, just as the electron paramagnetic resonance (EPR) result show that the signal strength of NiFe-SQ/NF-R is stronger than that of NiFe-LDH/NF-R under the same conditions (Supplementary Fig. 28). Detailed analytical fitting procedures are depicted in Supplementary Fig. 29. The removal of squaric acid ligands from the primary framework results in an increased presence of vacant sites in the hydroxyl oxide derivatives obtained through reconstruction. These vacancies can buffer the lattice distortion of the Fe site to reduce the dissolution tendency of Fe, thereby avoiding phase segregation of Fe.[35] Therefore, the presence of coordination vacancies within the NiFe-SQ/NF-R plays a pivotal role in safeguarding the integrity of the Fe sites, thereby contributing to its notable stability.

In addition to the coordination environment, the dynamic evolution of the catalytic structure and electrode interface microenvironment will also greatly influence the catalytic behavior of metal centers. This research delves into a detailed examination of the electrochemical structure evolution and interface microenvironment formation mechanism of NiFe-SQ/NF-R and NiFe-LDH/NF-R through in situ Raman and attenuated total reflection Fourier transform infrared spectroscopy (ATR-FTIR). Under alkaline conditions, the diffusion of OH$^-$ dominates the Ni(OH)$_2$ + OH$^- \leftrightarrow$ NiOOH+H$_2$O + e$^-$ reaction. By applying the Randles−Sevick equation, the effect of the scanning rate on the oxidation peak current density was investigated (Fig. 4a)[40]. The results show that NiFe-SQ/NF-R demonstrates improved OH$^-$ diffusion kinetics, which is a key element in facilitating the generation of NiOOH and improving catalytic activity. Considering the structural features of NiFe-SQ/NF-R, it is reasonable to speculate that the swift OH$^-$ diffusion capability stems from the external micron-scale channel structure and the increased interlamellar spacing resulting from internal Sq$^{2-}$
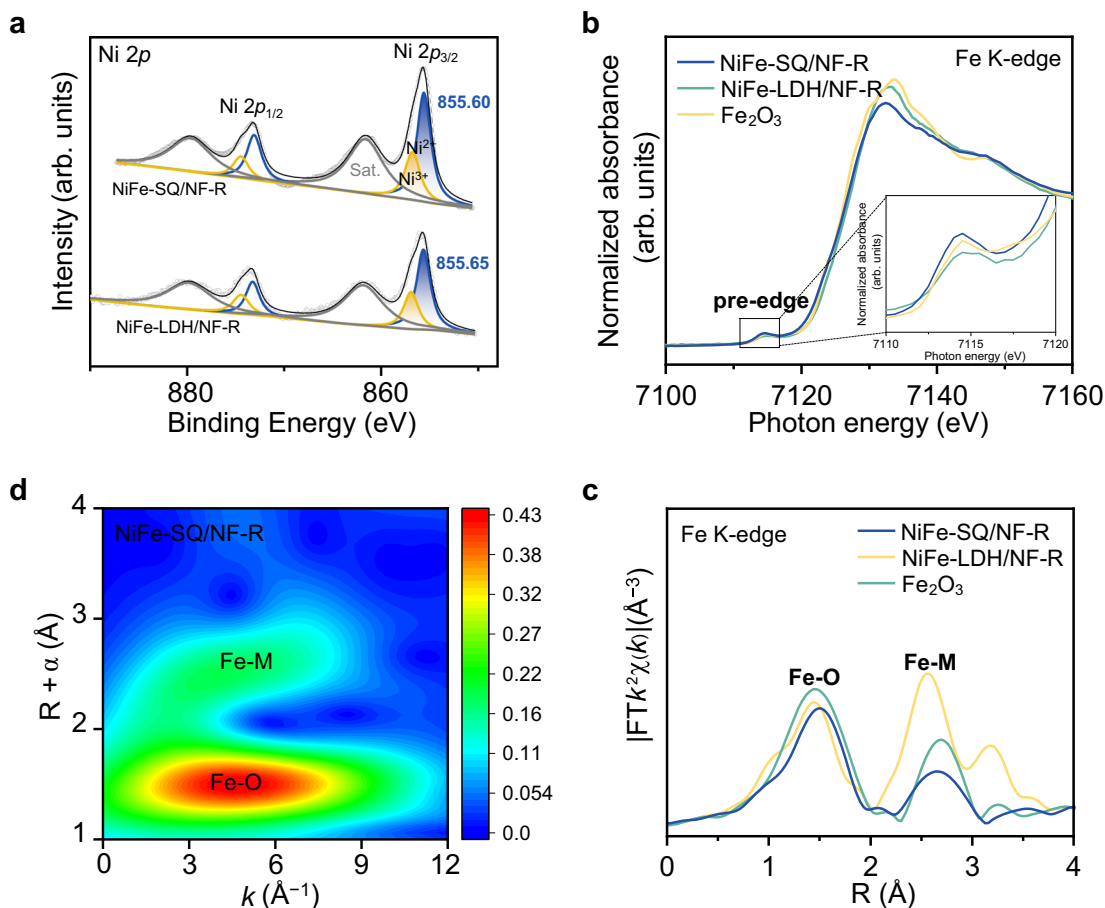
**Fig. 3 | Low saturation coordination configuration of Fe sites in NiFe-SQ/NF-R.**
**a** XPS spectra of NiFe-LDH/NF-R and NiFe-SQ/NF-R. **b** Fe $K$-edge XANES spectra for NiFe-LDH/NF-R and NiFe-SQ/NF-R. **c** Wavelet transform of Fe-$K$-edge EXAFS data of NiFe-SQ/NF-R. **d** FT-EXAFS curves at Fe $K$-edge collected for NiFe-LDH/NF-R and NiFe-SQ/NF-R. ($R$ is the distance from the central atom and $k$ is the wavelength.) Source data are provided as a Source Data file.

intercalation. In Fig. 4b, the initial NiFe-SQ/NF structure displays a prominent peak at 1492 $cm^{-1}$, which is indicative of the structural C−O bond (O−C−C−O$_{str}$) and represents the saturated coordination between squaric acid and the metal center. Following the CV-driven electrochemical reconstruction process, the O−C−C−O$_{str}$ peak vanished from the catalytic surface, while a newly O−C−C−O$_{ad}$ associated with Sq$^{2-}$ emerged at -1560 $cm^{-1}$ [41,42]. The wide peak at -3300 $cm^{-1}$ is associated with the O−H stretching vibration pattern of asymmetric hydrogen bonds resulting from the interaction of OH$^-$ with adsorbed Sq$^{2-}$. The magnitude of these peaks increases proportionally to the level of activation, as the incorporation of Sq$^{2-}$ leads to a gradual expansion of the Fe-doped NiOOH layer, facilitating enhanced interlayer diffusion and steady presence of more OH$^-$. Even after conducting 20 CV activation scans, the peaks at 1560 $cm^{-1}$ and 3300 $cm^{-1}$ remained present, suggesting the stable intercalation and adsorption of Sq$^{2-}$ between the layers of the sample. In the CV activation process of NiFe-LDH/NF, no obvious change in the peaks at about 3300 $cm^{-1}$ (Supplementary Fig. 30) was found, but the peaks of NiFe-SQ/NF-R were enhanced during the activation, further highlighting the important role of Sq$^{2-}$ in stabilizing OH$^-$. The structural evolution of NiFe-SQ/NF during the electrochemical reconstruction process can be deduced as follows: the alkali hydrolysis process first disrupts the coordination bond between the squaric acid ligand and the metal center, enabling the uncoordinated C−O group to establish an anchoring effect with OH$^-$ through hydrogen bonding. In addition, Sq$^{2-}$ interacts with M-OH (M: Fe or Ni) at the metal-catalyzed interface to create adsorption-bonded O−C−C−O$_{ad}$ for stable interlayer insertion. The analysis of the ATR-FTIR data further validates the evolution process of the structure,

supporting previous findings from spherical aberration electron microscopy. We employed an improved in-situ Raman electrochemical cell (Supplementary Fig. 31) to accurately examine the interfacial H$_2$O/OH$^-$ structure near the electrode surface. Three different hydrogen-bonded water structures are deconvolved: 4−HB·H$_2$O (-3200 $cm^{-1}$), 3−HB·H$_2$O/OH$^-$ (-3400 $cm^{-1}$), and 0−HB·H$_2$O (-3600 $cm^{-1}$).[22,43,44] Sq$^{2-}$ with four uncoordinated O* is able to form more complex hydrogen bond interactions with interfacial H$_2$O and OH$^-$ to regulate interfacial water structure. This resulted in distinct O-H stretching patterns observed in NiFe-SQ/NF-R samples in contrast to NiFe-LDH/NF-R (Fig. 4c, d). In Supplementary Fig. 32, the ratio of 4-HB·H$_2$O and 3-HB·H$_2$O on the NiFe-SQ/NF interface demonstrated a consistent increase with prolonged testing duration, while it exhibited a notable decrease on the NiFe-LDH/NF interface. These results suggest that the inserted Sq$^{2-}$ has the ability to regulate interfacial water and capture OH$^-$, which is conducive to alleviating local acidification during OER.

Changes in the interface alkalinity of NiFe-SQ/NF and NiFe-LDH/NF were observed through in situ Raman spectroscopy, utilizing the phosphoric acid-sensitive pH characteristics. The principle of this method is that as the pH value increases, the phosphate species can undergo the conversion of H$_3$PO$_4$ → H$_2$PO$_4^-$ → HPO$_4^{2-}$ → PO$_4^{3-}$ (illustration of Fig. 5a).[45] The electrolyte with a phosphate compound served as a pH probe during in situ Raman analysis. Through the correspondence between the characteristic Raman vibration peak of the phosphate species and pH, we can establish a linear relationship between pH and the vibration peak. This monitoring is crucial for understanding the local acidification micro-environment on Ni-Fe-based layered materials during anode testing, which is a notable issue that impacts activity and stability, particularly
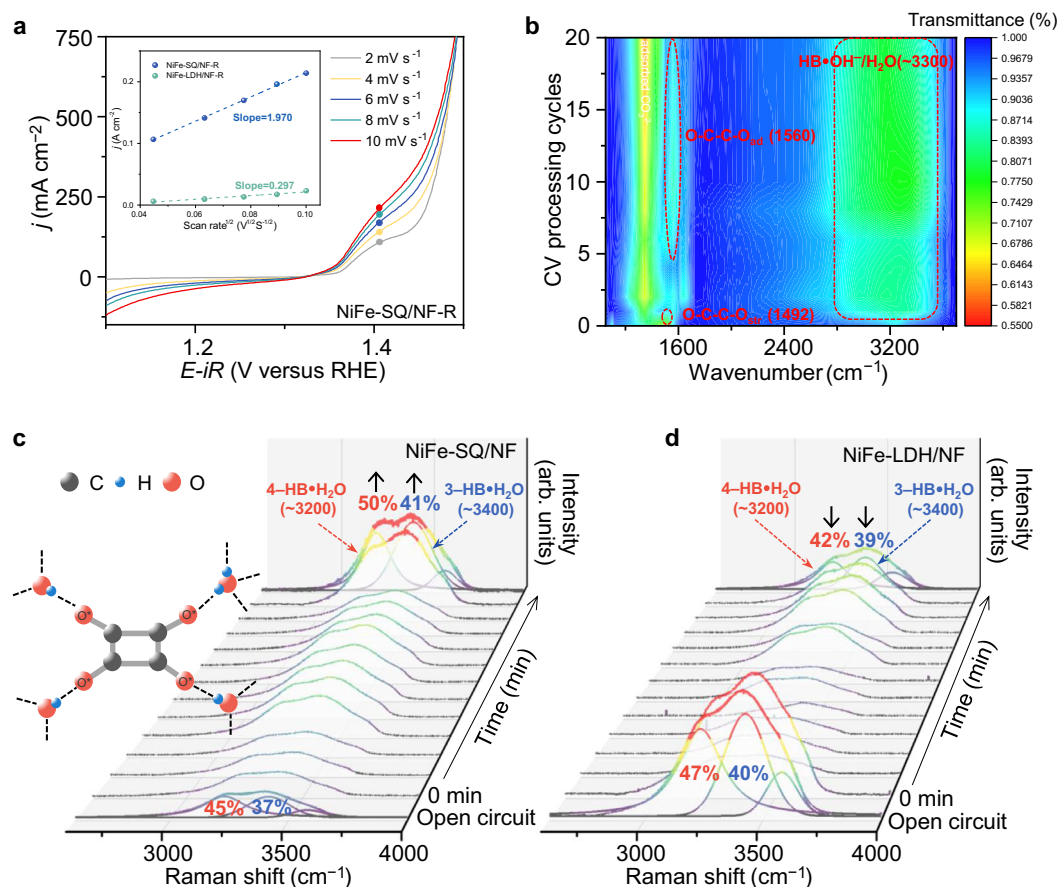
**Fig. 4 | Superior OH⁻ diffusion, trapping, and stabilization capabilities of NiFe-SQ/NF-R. a** LSV curves of NiFe-SQ/NF-R at different sweep speeds. **b** Contour plots of ATR-FTIR data of NiFe-SQ/NF after different CV scan cycles. In situ Raman spectra of **c** NiFe-SQ/NF and **d** NiFe-LDH/NF for water structures. Source data are provided as a Source Data file.

under large current density testing conditions. During in situ testing, spectral data were collected at 4-min intervals under a consistent current density of 10 mA cm⁻² in a solution of KOH and phosphoric acid at pH 12. By observing the variation of the characteristic peaks of $PO_4$ (936 cm⁻¹), $PO_3$ (990 cm⁻¹), and $P(OH)$ (857 cm⁻¹), we get the local pH values of the NiFe-LDH/NF and NiFe-SQ/NF. Low vibrational transition energy leads to a weak peak signal of $P(OH)$. Nevertheless, this minimal effect does not hinder the formulation of conclusions. It was found that rapid reduction of local pH from 12 to 8 in NiFe-LDH/NF was accomplished within a short duration of 12 min (Fig. 5a). This provides direct evidence that the layered structure of NiFe-LDH tends to promote an acidic microenvironment, pinpointing a key factor contributing to its limited large current stability. Surprisingly, during the initial 52 min of the examination, the regional pH of NiFe-SQ/NF exhibited constancy at 12, which then transitioned to 11 by the 56th min (Fig. 5b), with its acidification rate at the interface notably lagging behind that of NiFe-LDH (Fig. 5d). The primary factor contributing to this outcome is the tendency of the intercalation adsorbed $Sq^{2-}$ to trap and stabilize OH⁻. In Fig. 5c, two peaks at approximately 1554 and 1640 cm⁻¹ are identified, which are attributed to asymmetric C-O vibrations ((M·)C-O and C=O) of adsorbed $Sq^{2-}$ (O−C−C−O_{ad}), respectively. Over time, these peaks demonstrated a slight tendency towards augmentation, suggesting an increase in the presence of $Sq^{2-}$ adsorbed within the layers with the deepening of the reconstruction process. Therefore, the presence of intercalated adsorbed $Sq^{2-}$ is demonstrated to be pivotal in upholding localized interface alkalinity, thereby notably prolonging the catalytic lifespan by tenfold under high currents of 3.0 A cm⁻². As shown in Fig. 5e, based on the above analysis, it becomes evident that the sluggish surface acidification rate of NiFe-SQ/

NF stems from two key factors. First, in terms of surface structure composition, the dispersed micron-scale diffusion channels and expanded layer spacing directly facilitated the internal diffusion of OH⁻ and the outward transfer of H⁺. Second, when considering internal structural groups, $Sq^{2-}$ as "intermediaries", is adept at trapping and steadying OH⁻, thereby expediting the conversion of H⁺ and consequently delaying the emergence of a localized acidic microenvironment, thus sustaining heightened interface alkalinity. In short, this regulatory mechanism of interface alkalinity is particularly important for optimizing the local interfacial microenvironment under harsh conditions characterized by a high current.

## The theoretical source of enhanced catalytic activity

The enhancement of catalytic activity through the internal mechanism of interlaminar $Sq^{2-}$ anions was further investigated via spin polarization density functional theory (DFT) calculations. Peaks corresponding to $Ni(OH)_2$ (455, 530 cm⁻¹) and NiOOH (476, 553 cm⁻¹) are evident in Fig. 6a, suggesting that NiFe-SQ/NF underwent surface restructuring to facilitate the formation of NiOOH, a notably potent species. The electrochemical reconstruction processes of NiFe-LDH/NF and NiFe-SQ/NF led to the formation of Fe-doped NiOOH (Fe-NiOOH(NiFe-LDH/NF-R)) and Fe-doped NiOOH with intercalated $Sq^{2-}$ (Fe-NiOOH($Sq^{2-}$)(NiFe-SQ/NF-R)), respectively, which served as the primary active layers. After a rounded analysis, it is clear that the model architecture harbors promising active sites denoted as Ni−O−Fe−O−Ni and Ni−O−Ni−O−Ni. As shown in Supplementary Fig. 33, computational assessments were conducted to determine the optimal OER pathways for Fe-NiOOH($Sq^{2-}$)(NiFe-SQ/NF-R) and Fe-NiOOH(NiFe-LDH/NF-R) at these
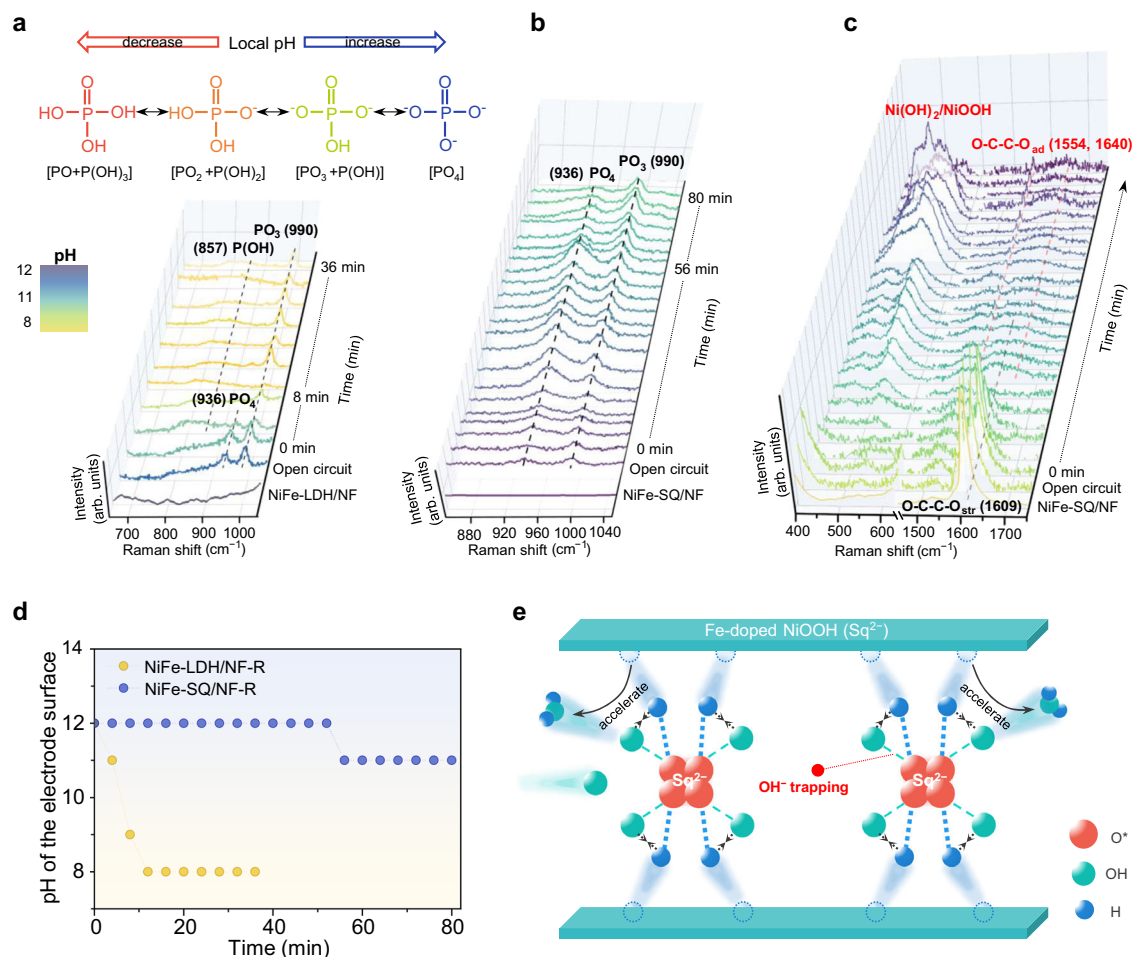
**Fig. 5 | Regulation mechanism of the intercalated $Sq^{2-}$ on interface alkalinity.** In situ Raman spectra of **a** NiFe-LDH/NF and **b** NiFe-SQ/NF in a solution of KOH and phosphoric acid at pH 12. (The illustration shows the structural transformation of phosphates at different pH values.) **c** In situ Raman spectra of NiFe-SQ/NF with background correction. **d** The change of interface pH with the test time. **e** A schematic illustration of the intercalated $Sq^{2-}$ trapping $OH^-$ to induce a highly alkaline interface. Source data are provided as a Source Data file.

designated active sites (Supplementary Data 1). For the Ni−O−Fe−O−Ni site in Fig. 6b, the rate-determining step (RDS) of the OER is the transition from *O to *OOH, and the barrier is reduced from 3.37 eV to 2.76 eV through the incorporation of $Sq^{2-}$ anions. This is because interlayer $Sq^{2-}$ increases the effective concentration of $OH^-$ near the active site through multiple hydrogen bonds interacting with $OH^-$, which facilitates the formation of key *OOH intermediates. Additionally, the deprotonation barrier of the *OOH step in Fe-NiOOH($Sq^{2-}$) (NiFe-SQ/NF-R) is notably lower at 0.01 eV than that in Fe-NiOOH(NiFe-LDH/NF-R), which is 1.07 eV. This result indicates that $Sq^{2-}$ accelerates the *OOH dehydrogenation process, which is due to both the unpaired O* sites and the captured $OH^-$ serve as proton acceptors to ensure the efficiency of the deprotonation process. In this study, the predominant active site for the OER was identified as the Ni−O−Fe−O−Ni site. This site is proposed to enable an $Sq^{2-}$ led efficient pathway, which supports the activation and stabilization of *OOH intermediates and assists in their deprotonation. Consequently, this mechanism reduces the reaction energy barrier and increases the catalytic effectiveness.

Upon examination of the density of states (DOS) images, it was noted that the electron state density of Fe-NiOOH($Sq^{2-}$)(NiFe-SQ/NF-R) surpasses that of Fe-NiOOH(NiFe-LDH/NF-R) at the Fermi level, suggesting that the intercalated $Sq^{2-}$ plays a notable role in enhancing electron transport efficiency (Fig. 6c). The electron state density of Fe within Fe-NiOOH($Sq^{2-}$)(NiFe-SQ/NF-R) is notably lower compared to Fe in Fe-NiOOH(NiFe-LDH/NF-R) across a wide energy range. This

observed disparity suggests a reduction in the electron cloud density surrounding the Fe orbital subsequent to the $Sq^{2-}$ intercalation procedure. This is consistent with the conclusion shown by the differential charge density map (Supplementary Fig. 34). The orbital state densities of Fe and O in Fe-NiOOH($Sq^{2-}$)(NiFe-SQ/NF-R) demonstrate closer overlapping resonances, leading to stronger electron interactions.[34,46] Consequently, our as-designed NiFe-SQ/NF-R catalytic interface facilitates a comprehensive improvement in the catalytic activity for OER.

## Discussion

In summary, we present a simple approach for controlling the local alkalinity of the interfacial microenvironment under large current conditions by incorporating steadily adsorbed $Sq^{2-}$ anions between the layers of Fe-doped NiOOH. Intercalated $Sq^{2-}$ facilitates the activation and stabilization of *OOH intermediates and assists in their deprotonation, thereby increasing catalytic activity. The captured $OH^-$, acting as potent proton receptors, facilitates the rapid consumption of $H^+$, postponing the formation of acidic microenvironments, thereby bolstering the durability of the material when subjected to high current conditions. As a result, the NiFe-SQ/NF-R we produced demonstrates a lower overpotential (284 mV at 1.0 A cm$^{-2}$), a decreased Tafel slope (50 mV dec$^{-1}$), and reliable long-term stability (700 h under 3.0 A cm$^{-2}$). This research successfully incorporated functional ligand-derived anions into layered materials, leading to enhanced performance in
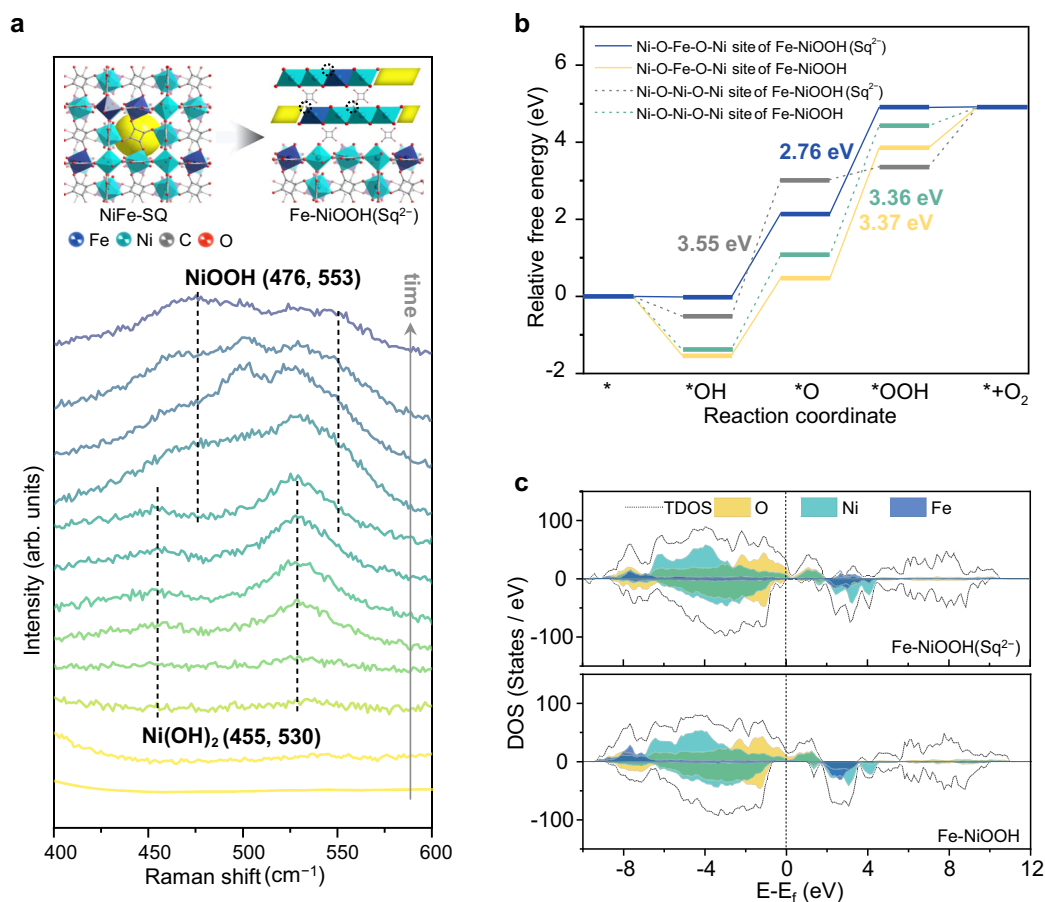
**Fig. 6 | Theoretical verification of improved OER catalytic activity. a** In situ Raman spectra of NiFe-SQ/NF. **b** Gibbs free energy diagrams of Fe-NiOOH(Sq$^{2-}$) (NiFe-SQ/NF-R) and Fe-NiOOH(NiFe-LDH/NF-R) at the Ni−O−Fe−O−Ni sites and Ni −O−Ni−O−Ni sites. **c** DOS of Fe-NiOOH(Sq$^{2-}$)(NiFe-SQ/NF-R) and Fe-NiOOH(NiFe-LDH/NF-R). Source data are provided as a Source Data file.

OER materials by minimizing the local acidic microenvironment and maintaining high interfacial alkalinity, especially under large current conditions.

## Methods

### Materials

Ferric nitrate nonahydrate (Fe(NO$_3$)$_3$·9H$_2$O, ≥99.9%), nickel nitrate hexahydrate (Ni(NO$_3$)$_2$·6H$_2$O, ≥98.0%), cobaltous nitrate hexahydrate (Co(NO$_3$)$_2$·6H$_2$O, ≥98.5%), polyvinylpyrrolidone (PVP K30, ≥99.8%), ammonium fluoride (NH$_4$F, ≥96.0%), urea (CO(NH$_2$)$_2$, ≥99.0%), acetone (CH$_3$COCH$_3$, ≥99.5%), ethanol (C$_2$H$_5$OH, ≥99.9%), hydrochloric acid (HCl, 36–38%) and potassium hydroxide (KOH, ≥85.0%) were purchased from Sinopharm Chemical Reagent Co., Ltd., Shanghai, China. 3,4-dihydroxy-3-cyclobutene-1,2-dione (squaric acid, C$_4$H$_2$O$_4$, ≥98.0%) was acquired from Macklin Chemical Reagent Co., Ltd., Shanghai, China. Nickel foam (NF) (aperture: 110 ppi, thickness: 1.5 mm) was obtained from Kunshan Lvchuang Electronic Technology Co., Ltd. Pt/C (20 wt%, Macklin Chemical Reagent Co. Ltd.) and Nafion (5 wt%, Sigma–Aldrich) were also used. Deionized water was used in all experiments. All the chemicals used in this study were of analytical grade and were used without further purification. All aqueous solutions in this experiment were prepared with deionized water (room temperature resistivity of 18.2 MΩ).

### Synthesis of NiFe-SQ/NF-R

NF (2.5 cm * 3.5 cm * 1.5 mm) was initially subjected to ultrasonic cleaning in acetone, hydrochloric acid (1 M), and ethanol, each for 15 min. Thorough removal of oxides and organic residues from the NF

surfaces played a crucial role in the preparation of the electrocatalysts for this study. Subsequently, the NF was placed in a solution comprising 0.3000 g of PVP, 2.5 mmol of squaric acid, 0.5 mmol of Fe(NO$_3$)$_3$·9H$_2$O, and 30 mL of deionized water. Then, the mixture was transferred to a 100 mL Teflon vessel sealed with a stainless autoclave, heated to 120 °C, and maintained for 6 h. The resulting dark green NiFe-SQ/NF sample was obtained after rinsing with deionized water and drying in a vacuum oven at 60 °C. Finally, NiFe-SQ/NF underwent electrochemical activation in 1 M KOH to yield NiFe-SQ/NF-R. The specific activation process involved cyclic voltammetry in a standard three-electrode configuration, with a scanning range of 0–1.488 V versus RHE, a scanning rate of 10 mV s$^{-1}$, and a total of 10 cycles.

### Synthesis of NiFe-LDH/NF-R

The process of synthesizing NiFe-LDH/NF-R closely mirrors that of NiFe-SQ/NF-R, differing primarily in replacing the solution with 1.0 mmol of Ni(NO$_3$)$_2$·6H$_2$O, 0.5 mmol of Fe(NO$_3$)$_3$·9H$_2$O, 2.5 mmol of NH$_4$F, 6 mmol of CO(NH$_2$)$_2$, and 30 mL of deionized water.

### Structural characterization

The crystal phase of the catalyst was analyzed using XRD with Cu $K\alpha$ radiation ($\lambda$ = 1.54 Å) on a Rigaku D/max-2500 pc apparatus. The morphological characteristics of the samples were examined by scanning electron microscopy (SEM) with a Hitachi S-4800 instrument. The elemental composition and distribution of the catalyst were evaluated using energy-dispersive spectroscopy in conjunction with a Hitachi S-4800 instrument. The powder samples were dissolved in dilute acid for inductively coupled plasma-optical emission

spectroscopy (ICP-OES) test (Agilent 5110 (OES)) to obtain the exact content of Fe and Ni elements. Electron paramagnetic resonance (EPR) data was collected on the German-Bruker-A300 spectrometer. Spherical aberration-corrected transmission electron microscopy (AC−TEM) images and elemental maps were obtained using an aberration-corrected transmission electron microscope (Titan Themis Cubed G2 300) operating at 300 kV. The contact angle of ultrapure water on the electrode was measured at room temperature by employing a dynamic contact angle system (JC2000C1). XPS data were calibrated to the C 1$s$ peak energy of 284.8 eV using a Thermo Fisher Scientific II spectrometer equipped with an Al Kα source (1486.6 eV). ATR-FTIR was conducted with a BRUKER ALPHA II infrared spectrometer. In situ Raman spectroscopy was performed in electrolytes of KOH and $H_3PO_4$ at pH 12 using the samples and platinum wire as the working and counter electrodes, respectively. The laser excitation wavelength during the measurements was 532 nm, a constant current density of 10 mA cm$^{-2}$ was maintained by the electrochemical workstation, and spectral data were collected every 4 min. The X-ray absorption fine structure energy spectrum (XAFS) was obtained at the Shanghai Synchrotron Radiation BL13SSW station (SSRF, 3.5 GeV, 220 mA, Si(111) twin). Data acquisition is carried out using a small detector under environmental conditions. The Athena module in the IFEFFIT package is used for standard XAFS data processing.

### Electrochemical measurements

This investigation examined the performance of various electrocatalysts in the OER utilizing a standard three-electrode configuration in an alkaline environment (KOH) with a GamryInterface 3000E workstation. The electrolyte employed in this investigation is 1 M KOH solution, exhibiting a pH of 13.6 ± 0.1. To maintain the purity and pH stability of the electrolyte, immediate utilization is recommended. The solution is prepared by dissolving a specific mass of solid potassium hydroxide in deionized water, adhering to the prescribed stoichiometric ratio. Short-term storage is permissible in a capped polypropylene container prior to experimentation. A polypropylene-based cell (50 mL) was utilized to minimize contamination from glassware in alkaline solutions. The synthesized electrocatalysts (1.0 cm$^2$), Pt sheet, and mercury oxide (Hg/HgO) electrode are used as working electrode, opposite electrode and reference electrode respectively. Standard new Hg/HgO electrodes are used to calibrate the working electrodes. Specifically, the electrode to be calibrated and the new Hg/HgO electrode are placed in the KOH electrolyte at the same time, and the open circuit voltage (OCP−T) of the system is tested after connecting the workstation respectively. If the potential difference remains stable within a 5 mV range, the working electrode is deemed calibrated and suitable for use. All potentials were converted to the reversible hydrogen electrode (RHE) utilizing the following equation:

$$E_{RHE} = E_{Hg/HgO} + 0.059 \times pH + 0.098V \qquad (1)$$

Linear sweep voltammetry (LSV) was carried out at a rate of 5.0 mV s$^{-1}$ with manual $iR$ compensation, unless otherwise stated. Specifically, the resistance of the system solution is tested first and compensated manually at a value of 95%. EIS tests spanned a frequency range of 10$^5$-0.1 Hz at 1.48 V versus RHE. The system solution resistance values of NiFe-SQ/NF-R, NiFe-LDH/NF-R and NF-R samples measured in this experiment are 0.80 ± 0.02, 0.89 ± 0.02 and 0.99 ± 0.02 Ω, respectively. The large current performance and stability were evaluated using a GamryInterface 5000E workstation assisted by stirring and automatic circulation refill devices. In this process, the electrochemical workstation acts as a potentiostat to automatically collect and store test data.

### Membrane electrode measurement

NiFe-SQ/NF-R (electrode area: 1.0 cm$^2$) and Pt/C (electrode area: 1.0 cm$^2$, mass loading: 0.5 mg cm$^{-2}$) were used as the anode (OER) and cathode (HER), respectively. KOH (1 M) was circulated through the membrane electrode at a flow rate of 50 mL min$^{-1}$. The anion exchange membrane (AEM) employed is Fumasep FAA-3-50, with dimensions of 1.3 * 1.3 cm and a thickness of 50 μm. Prior to utilization, the AEM is pretreated by immersion in a 0.5–1.0 M KOH solution for a duration of 12 h, followed by rinsing with deionized water. The full-cell OER performance was evaluated on a GamryInterface 5000E workstation at 25 °C.

### Density functional theory calculations

DFT calculations were conducted employing the Vienna ab initio simulation package (VASP) to explore the alkaline OER. The calculations were carried out using the Projector augmented wave method with a cutoff energy of 400 eV and the Perdew−Burke−Ernzerhof functional. To consider the impact of the 3$d$ electrons of the Ni and Fe atoms, the DFT + U method was utilized with effective U values of 5.5 eV[47] and 5.3 eV[48], respectively. Moreover, the DFT-D3 method was applied to correct for the influence of the 3$d$ electrons of Ni atoms and van der Waals interactions.[49] This study involved cleaving two layers of NiOOH (0 0 1) facets with a vacuum layer of 20 Å and incorporating 16% of the Ni atoms substituted with Fe atoms to form the Fe-doped NiOOH (Fe-NiOOH(NiFe-LDH/NF-R)) model. Furthermore, Sq$^{2-}$ was introduced between the layers to create Fe-doped NiOOH with an intercalated Sq$^{2-}$ (Fe-NiOOH(Sq$^{2-}$)(NiFe-SQ/NF-R)) model. All models underwent full relaxation with an energy convergence criterion of 10$^{-5}$ eV and a force convergence criterion of 0.02 eV Å$^{-1}$. The $\Gamma$ point was utilized in the K-point mesh, and the adsorption energy ($E_{ads}$) was computed using formula 2.

$$E_{ads} = E_{total} - E_{substrate} - E_{adsorbate} \qquad (2)$$

$E_{total}$, $E_{substrate}$ and $E_{adsorbate}$ represent the energies of the adsorption structure, substrate, and adsorbate, respectively. The free energies were calculated using the following formula 3:

$$G = E_{DFT} + ZPE - TS \qquad (3)$$

$G$, $E_{DFT}$, $ZPE$, and $TS$ represent the free energy, energy from DFT calculations, zero-point energy, and entropic contributions, respectively.

## Data availability

The data that support the plots within this paper are available from the corresponding author upon request. The source data generated in this study are provided in the Source Data file. Source data are provided with this paper.

## References

1.  Oener, S. Z., Foster, M. J. & Boettcher, S. W. Accelerating water dissociation in bipolar membranes and for electrocatalysis. *Science* **369**, 1099–1103 (2020).
2.  Yang, Y. et al. Electrocatalysis in alkaline media and alkaline membrane-based energy technologies. *Chem. Rev.* **122**, 6117–6321 (2022).
3.  Li, C. Q. & Baek, J. B. The promise of hydrogen production from alkaline anion exchange membrane electrolyzers. *Nano Energy* **87**, 106162 (2021).
4.  Ren, G. H., Zhou, M., Hu, P. J., Chen, J. F. & Wang, H. F. Bubble-water/catalyst triphase interface microenvironment accelerates photocatalytic OER via optimizing semihydrophobic OH radical. *Nat. Commun.* **15**, 2346 (2024).

5. Ge, W. X. et al. Dynamically formed surfactant assembly at the electrified electrode–electrolyte interface boosting $CO_2$ electro-reduction. *J. Am. Chem. Soc.* **144**, 6613–6622 (2022).

6. Zhao, J., Zhang, J. J., Li, Z. Y. & Bu, X. H. Recent progress on NiFe-based electrocatalysts for the oxygen evolution reaction. *Small* **16**, 2003916 (2020).

7. Liu, Z. Q. et al. Decoration of NiFe-LDH nanodots endows lower Fe-*d* band center of $Fe_1$-N-C hollow nanorods as bifunctional oxygen electrocatalysts with small overpotential gap. *Adv. Energy Mater.* **13**, 2203609 (2023).

8. He, Z. Y. et al. Activating lattice oxygen in NiFe-based (oxy) hydroxide for water electrolysis. *Nat. Commun.* **13**, 2191 (2022).

9. Lei, H. et al. Promoting surface reconstruction of NiFe layered double hydroxide for enhanced oxygen evolution. *Adv. Energy Mater.* **12**, 2202522 (2022).

10. Zhou, Y. N. et al. S-doped nickel-iron hydroxides synthesized by room-temperature electrochemical activation for efficient oxygen evolution. *Appl. Catal. B-Environ.* **292**, 120150 (2021).

11. Guo, H. N. et al. Zn-leaching induced rapid self-reconstruction of NiFe-layered double hydroxides for boosted oxygen evolution reaction. *Small* **20**, 2307069 (2024).

12. Fan, R. Y. et al. Directional regulating dynamic equilibrium to continuously update electrocatalytic interface for oxygen evolution reaction. *Chem. Eng. J.* **431**, 134040 (2022).

13. Jiang, W. et al. Composition-dependent morphology, structure, and catalytical performance of nickel–iron layered double hydroxide as highly-efficient and stable anode catalyst in anion exchange membrane water electrolysis. *Adv. Funct. Mater.* **32**, 2203520 (2022).

14. Zhou, D. J. et al. NiFe hydroxide lattice tensile strain: enhancement of adsorption of oxygenated intermediates for efficient water oxidation catalysis. *Angew. Chem. Int. Ed.* **58**, 736–740 (2019).

15. Zhang, Y. Y. et al. Hydrogen-bond regulation of the microenvironment of Ni(II)-porphyrin bifunctional electrocatalysts for efficient overall water splitting. *Adv. Mater.* **35**, 2210727 (2023).

16. Li, R. P. et al. Construction of self-supporting NiCoFe nanotube arrays enabling high-efficiency alkaline oxygen evolution. *ACS Appl. Mater. Interfaces* **14**, 54758–54768 (2022).

17. Li, Z. et al. High-density cationic defects coupling with local alkaline-enriched environment for efficient and stable water oxidation. *Angew. Chem. Int. Ed.* **62**, e202217815 (2023).

18. Chen, R. et al. Layered structure causes bulk NiFe layered double hydroxide unstable in alkaline oxygen evolution reaction. *Adv. Mater.* **31**, 1903909 (2019).

19. Wang, Q. Y. et al. Coupling nano and atomic electric field confinement for robust alkaline oxygen evolution. *Angew. Chem. Int. Ed.* **63**, e202405438 (2024).

20. Zhang, X. et al. A simple synthetic strategy toward defect-rich porous monolayer NiFe-layered double hydroxide nanosheetsfor efficient electrocatalytic water oxidation. *Adv. Energy Mater.* **9**, 1900881 (2019).

21. Malek, A., Xue, Y. R. & Lu, X. Dynamically restructuring $Ni_xCr_yO$ electrocatalyst for stable oxygen evolution reaction in real seawater. *Angew. Chem. Int. Ed.* **62**, e202309854 (2023).

22. Ram, R. et al. Water-hydroxide trapping in cobalt tungstate for proton exchange membrane water electrolysis. *Science* **384**, 1373–1380 (2024).

23. Yu, X. X. et al. Superaerophobic" nickel phosphide nanoarray catalyst for efficient hydrogen evolution at ultrahigh current densities. *J. Am. Chem. Soc.* **141**, 7537–7543 (2019).

24. Zhao, H. Y. et al. Precipitation/dissolution equilibrium to achieve trace iron doping on the surface of $\beta$-$Ni(OH)_2$ for electrocatalytic oxygen evolution. *Fuel* **332**, 125780 (2023).

25. Kandambeth, S. et al. Unveiling chemically robust bimetallic squarate-based metal–organic frameworks for electrocatalytic oxygen evolution reaction. *Adv. Energy Mater.* **13**, 2202964 (2023).

26. Zheng, X. Q. et al. Optimized sieving effect for ethanol/water separation by ultramicroporous MOFs. *Angew. Chem. Int. Ed.* **62**, e202216710 (2023).

27. Zhang, L. et al. A robust squarate-cobalt metal–organic framework for $CO_2$/$N_2$ separation. *ACS Appl. Mater. Interfaces* **15**, 30394–30401 (2023).

28. Ding, H., Liu, H. F., Chu, W. S., Wu, C. Z. & Xie, Y. Structural transformation of heterogeneous materials for electrocatalytic oxygen evolution reaction. *Chem. Rev.* **121**, 13174–13212 (2021).

29. Zhang, R. R. et al. Tracking the role of defect types in $Co_3O_4$ structural evolution and active motifs during oxygen evolution reaction. *J. Am. Chem. Soc.* **145**, 2271–2281 (2023).

30. Georgopoulos, S. L., Milán-Garcés, E. A., Sant'Ana, A. C., Andrade, G. F. S. & Oliveira, L. F. C. Analysis of squaric acid and its complex with copper(II) ions adsorbed on silver nanoparticle surfaces surface-enhanced Raman spectroscopy. *Vib. Spectrosc.* **87**, 99–103 (2016).

31. Sant'Ana, A. C., Santos, P. S. & Temperini, M. L. A. The adsorption of squaric acid and its derived species on silver and gold surfaces studied by SERS. *J. Electroanal. Chem.* **571**, 247–254 (2004).

32. Wu, Y. J. et al. Evolution of cationic vacancy defects: a motif for surface restructuration of OER precatalyst. *Angew. Chem. Int. Ed.* **60**, 26829–26836 (2021).

33. Bodhankar, P. M., Sarawade, P. B., Singh, G., Vinu, A. & Dhawale, D. S. Recent advances in highly active nanostructured NiFe LDH catalyst for electrochemical water splitting. *J. Mater. Chem. A* **9**, 3180 (2021).

34. Li, W. L. et al. A bio-inspired coordination polymer as outstanding water oxidation catalyst via second coordination sphere engineering. *Nat. Commun.* **10**, 5074 (2019).

35. Lin, X. J. et al. Bioinspired trimesic acid anchored electrocatalysts with unique static and dynamic compatibility for enhanced water oxidation. *Nat. Commun.* **14**, 6714 (2023).

36. Liu, D. P. et al. A template editing strategy to create interlayer-confined active species for efficient and durable oxygen evolution reaction. *Adv. Mater.* **35**, 2203420 (2023).

37. Chung, D. Y. et al. Dynamic stability of active sites in hydr(oxy)oxides for the oxygen evolution reaction. *Nat. Energy* **5**, 222–230 (2020).

38. Wang, Y. et al. Facet engineering and pore design boost dynamic Fe exchange in oxygen evolution catalysis to break the activity–stability trade-off. *J. Am. Chem. Soc.* **145**, 20261–20272 (2023).

39. Peng, L. S. et al. Atomic cation-vacancy engineering of NiFe-layered double hydroxides for improved activity and stability towards the oxygen evolution reaction. *Angew. Chem. Int. Ed.* **60**, 24612–24619 (2021).

40. Hou, S. J. et al. Metamorphosis of heterostructured surface-mounted metal–organic frameworks yielding record oxygen evolution mass activities. *Adv. Mater.* **33**, 2103218 (2021).

41. Cheuquepán, W., Martínez-Olivares, J., Rodes, A. & Orts, J. M. Squaric acid adsorption and oxidation at gold and platinum electrodes. *J. Electroanal. Chem.* **819**, 178–186 (2018).

42. Cheuquepán, W., Rodes, A., Orts, J. M. & Feliu, J. M. Spectro-electrochemical and density functional theory study of squaric acid adsorption and oxidation at gold thin film and single crystal electrodes. *J. Phys. Chem. C* **122**, 22352–22365 (2018).

43. Wang, Y. H. et al. In situ Raman spectroscopy reveals the structure and dissociation of interfacial water. *Nature* **600**, 81–85 (2021).

44. Li, C. Y. et al. In situ probing electrified interfacial water structures at atomically flat surfaces. *Nat. Mater.* **18**, 697–701 (2019).

45. Lu, S. S., Zhang, Z. P., Zhang, B. & Shi, Y. M. Insight into the change in local pH near the electrode surface using phosphate species as the probe. *J. Phys. Chem. Lett.* **14**, 10457–10462 (2023).

46. Shi, G. D. et al. Constructing Cu-C bonds in a graphdiyne–regulated Cu single-atom electrocatalyst for $CO_2$ reduction to $CH_4$. *Angew. Chem. Int. Ed.* **61**, e202203569 (2022).

47. Tkalych, A. J., Zhuang, H. L. & Carter, E. A. A Density Functional + U Assessment of oxygen evolution reaction mechanisms on β-NiOOH. *ACS Catal.* **7**, 5329–5339 (2017).
48. Zhou, L. Y. et al. Quantitatively evaluating activity and number of catalytic sites on metal oxide for ammonium perchlorate decomposition. *AIChE J.* **68**, e17582 (2022).
49. Grimme, S., Antony, J., Ehrlich, S. & Krieg, H. A consistent and accurate ab initio parametrization of density functional dispersion correction (DFT-D) for the 94 elements H-Pu. *J. Chem. Phys.* **132**, 154104 (2010).

## Acknowledgements

## Author contributions

B.D. and Y.C. conceived the paper and directed the research. R.F., F.W., and Y.Z. designed and carried out the experiments. S.L. contributed to the in situ Raman spectra. B.D. and Y.C. performed the density functional theory calculations. M.H. analyzed the synchrotron radiation data. B.Z. provide discussion and sorted the writing ideas. R.F. wrote the paper. B.D. and B.Z. revised the manuscript with comments from all the authors.

## Competing interests

The authors declare no competing interests.

## Additional information

**Supplementary information** The online version contains supplementary material available at https://doi.org/10.1038/s41467-025-58623-7.

**Correspondence** and requests for materials should be addressed to Yongming Chai, Bin Dong or Bin Zhang.

**Peer review information** *Nature Communications* thanks Feifei Jia and the other anonymous reviewer(s) for their contribution to the peer review of this work. A peer review file is available.

**Reprints and permissions information** is available at http://www.nature.com/reprints

**Publisher's note** Springer Nature remains neutral with regard to jurisdictional claims in published maps and institutional affiliations.